ACS OMEGA

http://pubs.acs.org/journal/acsodf

Article

Low Toxicity, High Resolution, and Red Tissue Imaging in the Vivo of Yb/Tm/GZO@SiO_2 Core−Shell Upconversion Nanoparticles

Yandong Bai,* Yuemei Li, Rui Wang, and Yongmei Li

Cite This: *ACS Omega* 2020, 5, 5346−5355

Read Online

ACCESS | Metrics & More | Article Recommendations | Supporting Information

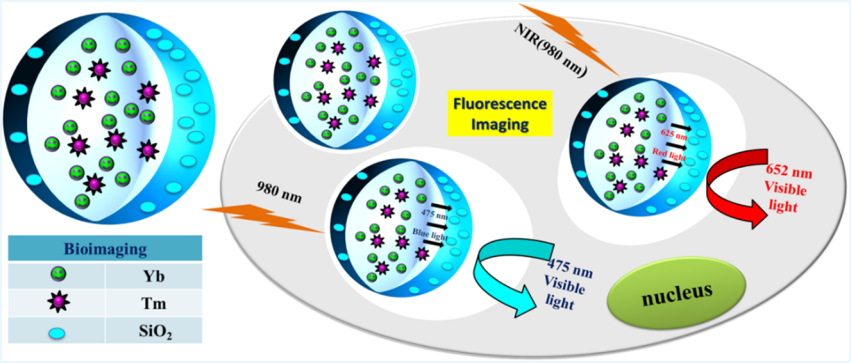

ABSTRACT: Lanthanide-doped upconversion nanoparticles (UCNPs) have attracted great attention in bioimaging applications. However, the stability and resolution of bioimaging based on UCNPs should be further improved. Herein, we synthesized SiO_2-coated Ga(III)-doped ZnO (GZO) with lanthanide ion Yb(III) and Tm(III) (Yb/Tm/GZO@SiO_2) UCNPs, which realized red fluorescence imaging in heart tissue. With increasing injection concentrations of Yb/Tm/GZO@SiO_2 (1−10 mg/kg), the red fluorescence imaging intensity of heart tissue gradually increased. Moreover, the experimental results of toxicity in vitro and histological assessments of representative organs in vivo were studied, indicating that Yb/Tm/GZO@SiO_2 UCNPs had low biological toxicity. These results proved that Yb/Tm/GZO@SiO_2 can be used as a probe for fluorescence imaging in vivo.

INTRODUCTION

Fluorescence imaging has attracted great attention in biological applications due to its high resolution and sensitivity.[1−3] Excellent in vivo and in vitro fluorescence imaging of cells requires some key factors such as a low imaging background, high fluorescence efficiency, and good imaging of photostability. However, the excitation source of traditional fluorescence imaging is ultraviolet or visible light, which has interference from autofluorescence and strong absorption.[4,5] It is well known that the near-infrared (NIR) region from 750 to 1000 nm is one of the "optical transmission windows".[1,6] Fluorescence imaging in vitro and in vivo excited in the NIR light has some advantages, such as low light scattering, deep light penetration, and a high signal-to-noise ratio.[7−10] Conventional NIR chromophores are organic dyes and quantum rods (QDs). However, organic dyes have poor photostability and toxicity, which significantly limit their application in biological fluorescent probes.[11−13]

Lanthanide-doped (Ln^{3+}, such as Yb^{3+}, Tm^{3+}, Er^{3+}, Ho^{3+}) upconversion nanoparticles (UCNPs) are a kind of emerging biological materials.[14−21] Upconversion luminescence (UCL) is anti-Stokes emission, which can convert to ultraviolet (UV) or visible (vis) emission via absorbing near-infrared (NIR) light. UCNPs based on their unique properties have been considered an important material for bioimaging applications.[22−28] Biological fluorescent probes based on lanthanide-doped UCNPs can be excited using 750−1000 nm NIR light.[29−33] Therefore, UCNPs show little absorption to biological components such as lipids and hemoglobin, which significantly improves deep tissue penetration and the signal-to-noise ratio.[34−38] It is challenging to develop a fluorescent probe with high UCL efficiency and good stability for bioimaging in living cells. In fact, the host has an important influence on UCL properties.[39−42] An oxide host has high chemical stability and thermal stability compared to fluorides. Choosing suitable oxides with low phonon energy as the host can increase the UCL intensity and fluorescence stability. For example, zinc oxide (ZnO) has been identified as a good host candidate due to its long-term stability, low toxicity, and wide direct gap.[43−46]

Received: December 19, 2019
Accepted: February 19, 2020
Published: March 2, 2020

https://dx.doi.org/10.1021/acsomega.9b04381
ACS Omega 2020, 5, 5346−5355

Scheme 1. Schematic Representation of the Imaging Mechanism of the Live Cell with Injection of UCNPs

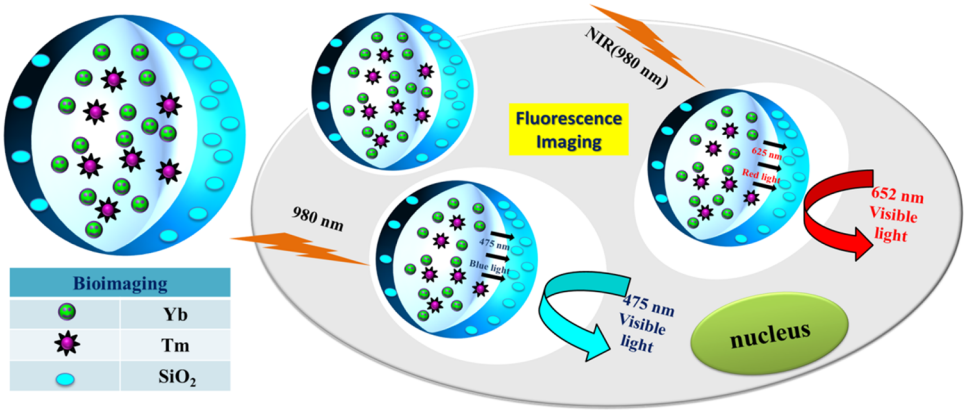

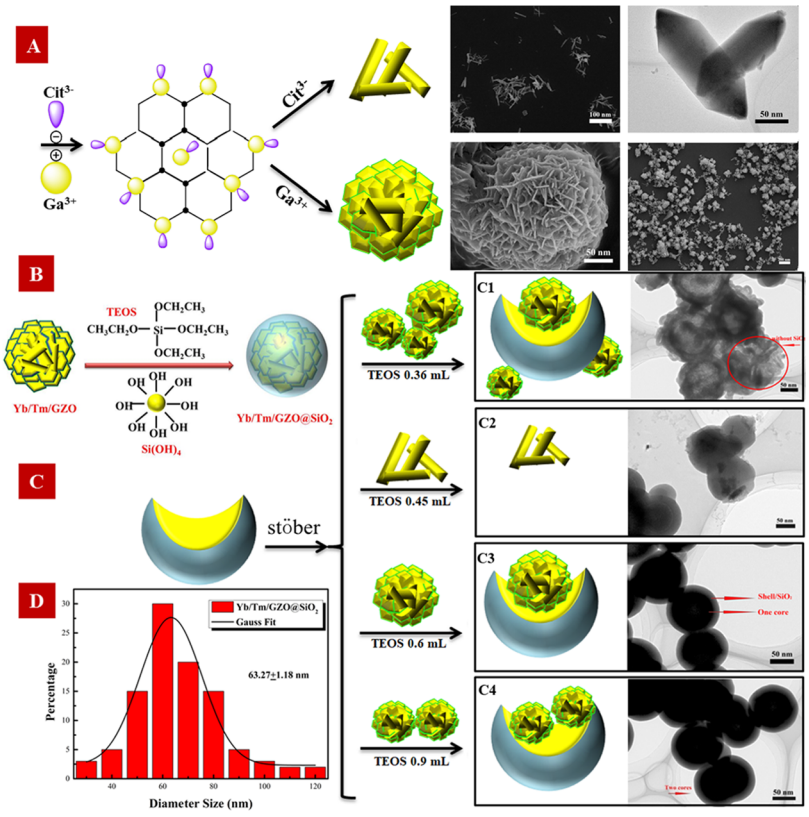

Figure 1. (A) SEM and TEM characterization of Yb/Tm/GZO (Ga: 10 mol %, Yb: 7 mol %, Tm: 0.5 mol % mol %) UCNPs. (B) Synthesis process of the Yb/Tm/GZO@SiO_2 core/shell structure. (C) TEM images of Yb/Tm/GZO@SiO_2 with different contents of TEOS from 0.36 to 0.90 mL. (D) Size distribution of Yb/Tm/GZO@SiO_2 with 0.60 mL of TEOS by gauss fitting.

However, it is still a big challenge to achieve high-resolution fluorescence imaging with UCNPs. The most common interaction between UCNPs and cells has a large influence on the toxicity and cellular localization of UCNPs. It has been reported that nanoparticles usually entered the cell through endocytosis.[47,48] The four mechanisms of endocytosis are: (i) micropinocytosis (size >1 μm), (ii) clathrin-mediated endocytosis (60 nm < size < 120 nm), (III) caveolae-mediated endocytosis (size <60 nm), and (iv) caveolae-independent endocytosis. Therefore, UCNPs can enter the cell via the coated surface on UCNPs.[49−51] Coating of UCNPs with silica shell as an effective method can improve the biocompatibility of nanoparticles. The SiO_2 shell prevents the direct interaction of UCNPs with biomolecules. Meanwhile, lanthanide ions on the surface of UCNPs show no luminescence emission, due to which these rare-earth ions are less perturbed by the degenerated crystalline fields of the host interfaces. Upon silica coating, cooperative crystalline fields are formed between the core surfaces and the coated shells, which excites the "dormant" Ln^{3+} ions (nonluminance Ln^{3+} ions) on the surface of nanoparticles.[52] The silica-coated surface not only improves the colloidal stability and prevents nonspecific cell uptake but also enhances the UCL efficiency.[53] Despite recent success in Yb/Tm co-doped UCNPs NIR region (about 800 nm) emission bioimaging, in vivo imaging with red emission had no establish at low pumping power due to low red UC quantum efficiency.

https://dx.doi.org/10.1021/acsomega.9b04381
ACS Omega 2020, 5, 5346−5355

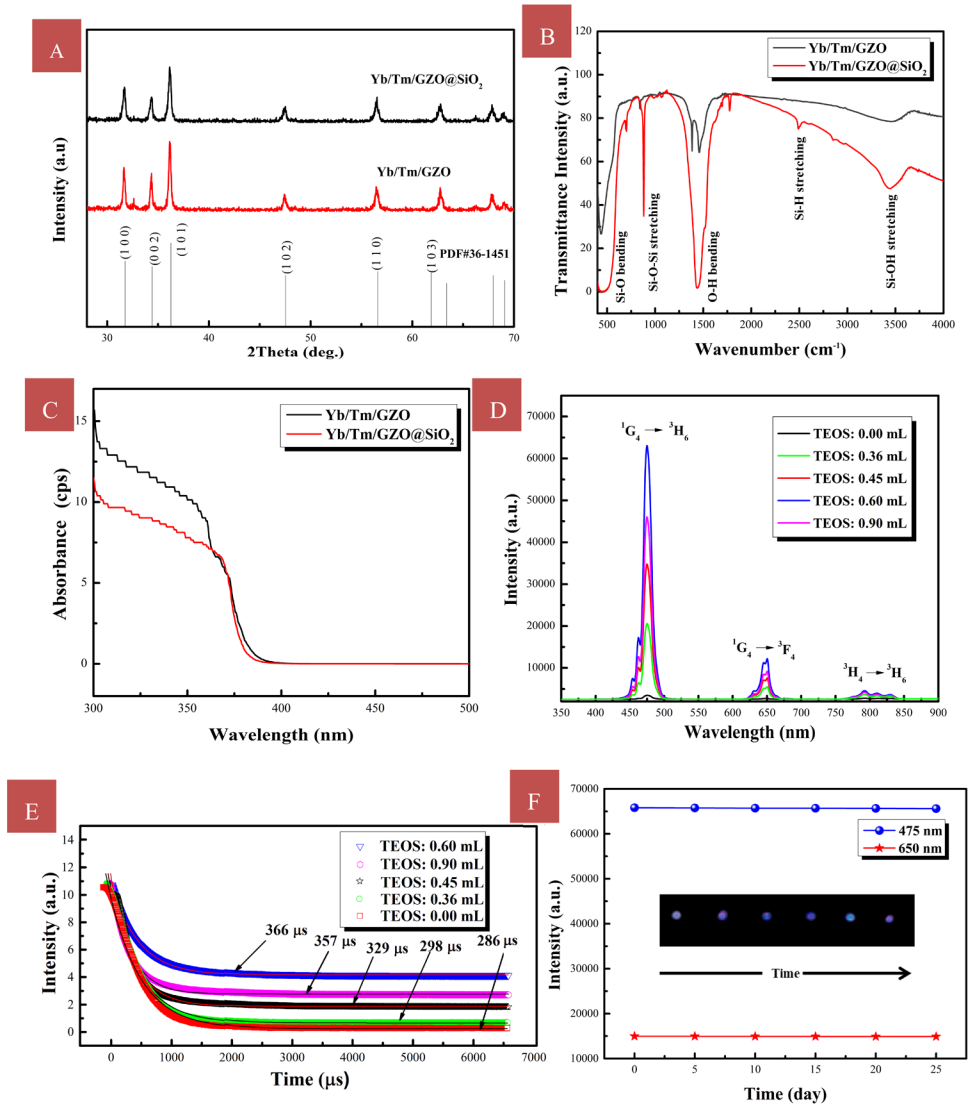

Figure 2. (A) X-ray diffraction spectra of Yb/Tm/GZO and Yb/Ym/GZO@SiO_2 nanoparticles. (B) FTIR spectra of Yb/Tm/GZO and Yb/Ym/GZO@SiO_2 nanoparticles. (C) Ultraviolet−visible (UV−vis) absorption spectra of Yb/Tm/GZO and Yb/Tm/GZO@SiO_2 nanoparticles. (D) Upconversion luminescence spectra of Yb/Tm/GZO@SiO_2 with different TEOS contents. (E) Decay lifetime for the 650 nm band for Yb/Tm/GZO@SiO_2 with different TEOS concentrations from 0 to 0.9 mL. (F) UCL intensities of Yb/Tm/GZO@SiO_2 (TEOS: 0.6 mL) with different assembly times from 0 to 25 days at room temperature; the inset shows the digital photographs of Yb/Tm/GZO@SiO_2 (TEOS: 0.6 mL) with different assembly times from 0 to 25 days.

In this work, the influence of relative concentrations of the silica coated on Yb/Tm/GZO (UCNPs) was investigated. Compared to the tetraethyl orthosilicate (TEOS)-free sample, the UCL intensity of Yb/Tm/GZO@SiO_2 increased about 13 times compared to that of Yb/Tm/ZnO UCNPs. The red UC quantum efficiency of Yb/Tm/GZO@SiO_2 was as high as 1.0 ± 0.1% under excitation with a low power density of ∼0.3 W/cm^2. The red UCL imaging of heart tissue treated with Yb/Tm/GZO@SiO_2 was achieved under 980 nm excitation. With the increase of the injection concentrations of Yb/Tm/GZO@SiO_2, red fluorescence imaging of heart tissue gradually increased. Moreover, we proved that Yb/Tm/GZO@SiO_2 had low toxicity in vitro and in vivo.

RESULTS AND DISCUSSION

As shown in Scheme 1, Yb/Tm/GZO@SiO_2 core/shell nanoparticles entered the cytoplasm via endocytosis. Upon 980 nm excitation, Yb^{3+}/Tm^{3+} ions were excited and radiated UCL, realizing red (650 nm) light bioimaging.

Synthesis and Characterization. Yb/Tm/GZO UCNPs were synthesized by the hydrothermal method. Cit^{3-} served as a structure regulating the size and morphology of Yb/Tm/GZO UCNPs. Figure 1A shows the scanning electron microscopy (SEM) images of Yb/Tm/GZO UCNPs. These Yb/Tm/GZO UCNPs exhibited structures of peony flowers and had good dispersibility. The silica coating on UCNPs can reduce the surface defects and improve the colloidal stability. Yb/Tm/GZO@SiO_2 was synthesized via the Stöber method with increasing tetraethyl orthosilicate (TEOS) concentrations from 0.36 to 0.90 mL (Figure 1B). The transmission electron microscopy (TEM) images of Yb/Tm/GZO@SiO_2 with different TEOS concentrations are shown in Figure 1C. With 0.36 mL of TEOS, core−shell structures were not completely obtained (see Figure 1C1). With increasing TEOS concentrations, Yb/Tm/GZO@SiO_2 with core−shell structure was

https://dx.doi.org/10.1021/acsomega.9b04381
ACS Omega 2020, 5, 5346−5355

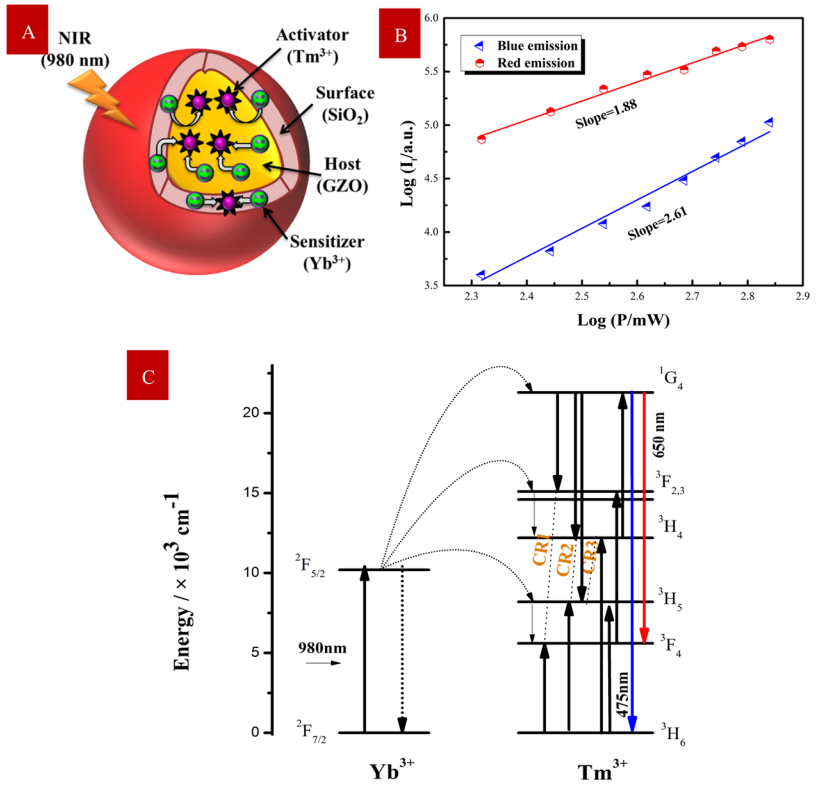

Figure 3. (A) Scheme of the proposed nanostructure. (B) Corresponding log (UC intensity)−log (excitation power) curve of Yb/Tm/GZO@SiO_2 nanoparticles. (C) Proposed energy transfer mechanism of Yb/Tm/GZO@SiO_2 under 980 nm excitation.

obtained, as demonstrated in Figure 1C2−C3. The size was 63.27 ± 1.18 nm at 0.60 mL of TEOS, 12 nm larger than the core (see Figure 1D). This result was obtained by measuring a total of 80 nanoparticles from four TEM images. With increasing TEOS up to 0.9 mL, obvious two cores were coated by the SiO_2 shell (Figure 1C4). These results indicate that the core−shell structure can be controlled in Yb/Tm/GZO@SiO_2 by varying the concentration of TEOS.

Optical Properties. The X-ray diffraction (XRD) patterns of Yb/Tm/GZO and Yb/Tm/GZO@SiO_2 are shown in Figure 2A. The diffraction peaks matched those of the hexagonal ZnO nanoparticles (JCPDs card no. 36-1541). The wide diffraction peaks due to amorphous SiO_2 were not found, suggesting that the SiO_2 coating showed no change in the phase of Yb/Tm/GZO UCNPs. To determine the successful preparation of the Yb/Tm/GZO@SiO_2 core−shell structure UCNPs, characteristic functional groups of Yb/Tm/GZO and Yb/Tm/GZO@SiO_2 were examined via Fourier transform infrared (FTIR) spectrometry. As shown in Figure 2B, the bands at 496 and 1495 cm^{-1} were ascribed to the Zn−O and O−H bending in the spectra of both Yb/Tm/GZO and Yb/Tm/GZO@SiO_2, respectively. In the Yb/Tm/GZO@SiO_2 system, bands at 955 and 725 cm^{-1} were associated with the symmetric and asymmetric stretching vibrations of the Si−O−Si group, respectively. The bands at 2490 and 3490 cm^{-1} corresponded to the stretching vibrations of the Si−H and Si−O−H groups, respectively.[45] These results proved that SiO_2 was successfully coated on UCNPs. Ultraviolet−visible (UV−vis) absorption spectra of Yb/Tm/GZO and Yb/Tm/GZO@SiO_2 were also recorded, as shown in Figure 2C. Compared to the UV−vis absorption edge of Yb/Tm/GZO UCNP, the absorption band edge of Yb/Tm/GZO@SiO_2 showed a blue shift, indicating that the energy for the 2p orbital transition of O^{2-} ions increased. The SiO_2 coating reduced the surface defect of Yb/Tm/GZO and thus bind free electrons transfer, which increased the energy absorbed for the electron transition in Yb/Tm/GZO@SiO_2.

To verify the effect of SiO_2 coating on UCL intensity, the UCL spectra of Yb/Tm/GZO@SiO_2 with different TEOS contents were recorded, as shown in Figure 2D. In comparison to the TEOS-free sample, the blue and red UCL intensities had been significantly enhanced with increasing TEOS content. Particularly, when the content of TEOS was 0.60 mL, UCL intensities were about 13 times higher than that of Yb/Tm/GZO. The red upconversion absolute quantum yield (QY) of Yb/Tm/GZO@SiO_2 was obtained by the integrating sphere to be 1.0 ± 0.1% with 0.6 mL of TEOS. This high absolute QY for red upconversion emission was achieved at a low excitation density (0.3 W/cm^2), indicating that Yb/Tm/GZO@SiO_2 UCNPs showed a great promising application in bioimaging. Moreover, with increasing TEOS concentration, the decay lifetimes of red UCL (650 nm) increased from 286 to 366 μs (Figure 2E). With increasing TEOS content, surface defects of UCNPs decreased. Meanwhile, the linear relationship between surface vibrations and SA/Vol can be represented as quenchers ([Q]) (eq 1).

$$[Q] = \frac{\text{surface defects}}{\frac{\text{SA}}{\text{Vol}}} \quad (1)$$

When the surface defects decreased, [Q] is significantly decreased. The decay lifetime was described using the Stern−Volmer (eq 2).

$$\frac{1}{\tau} = \frac{1}{\tau_0} + k_q[Q] \quad (2)$$

https://dx.doi.org/10.1021/acsomega.9b04381
ACS Omega 2020, 5, 5346−5355

where τ is the decay lifetime with quenchers, τ_0 is the observed decay lifetime without quenchers, k_q is the rate constant of the quencher, and τ_0 represents an ideal condition and can be regarded as a constant. The positive proportion relationship between $1/\tau$ and $[Q]$ shows that $[Q]$ decreased when the decay lifetime increased. A high decay lifetime can be achieved with increasing TEOS. In addition, considering that the SiO_2 shell had an influence on the UCL intensity of UCNPs, the UCL properties of Yb/Tm/GZO@SiO_2 were investigated at different times from 0 to 25 days at room temperature. Figure 2F shows that the UCL intensities of Yb/Tm/GZO@SiO_2 had no change with the extension of times, which indicated that the SiO_2 shell greatly maintained the stability of core−shell nanoparticles.

To validate that SiO_2 coating had an effect on Yb/Tm/GZO UCL properties, the upconversion transfer mechanism of the Yb/Tm/GZO@SiO_2 core/shell system was determined. In Figure 3C, the blue UCL can be ascribed to radiative energy transfer from the $^1G_4$ to $^3H_6$ state of the Tm^{3+} ion. The red UCL can be attributed to radiative energy transfer from the $^1G_4$ to $^3F_4$ state of the Tm^{3+} ion. To further confirm the photon excitation process of core−shell nanoparticles, the dependence of the UCL intensity of Yb/Tm/GZO@SiO_2 nanoparticles on the power density was examined. As shown in Figure 3B, the slopes of UCL at wavelengths of 475 and 650 nm were 2.61 and 1.88, respectively. This was because the blue and red UCL emissions of Tm^{3+} were attributed to the three-photon process and two-photon process, respectively. Compared to the number of photons in Yb/Tm/GZO (Figure S1), the number of photons in Yb/Tm/GZO@SiO_2 decreased. Without SiO_2 shell coating, Tm^{3+}-ion-doped GZO can be excited to produce UCL emission, owing to the perturbation of the crystal field in the GZO system. Because of this, the boundary was weakly disturbed by the degenerate crystal field on the surface of GZO nanoparticles. The Tm^{3+} ions near and embedded in the surface layer of the GZO host did not produce UCL emission and are called dormant ions. SiO_2 coating of Yb/Tm/GZO resulted in the interaction of the degenerated crystal field on the surface of GZO and the coordination field produced. These reduced the selection rule of radiative transitions of the dormant rare-earth ions (Yb^{3+}/Tm^{3+}). The dormant ions can be activated. The excited dormant ions were called the "activated" rare-earth ions. As shown in Figure 3A, SiO_2 coating on the surface of Yb/Tm/GZO reduced the selection rule of radiative transitions and the dormant Tm^{3+}/Yb^{3+} ions became the new luminescence centers. Owing to the large specific surface of nanoparticles, a large number of new luminescent centers were formed on the surface of GZO nanoparticles. The UCL intensity of Yb/Tm/GZO@SiO_2 nanoparticles enhanced compared to that of Yb/Tm/GZO. The SiO_2 shell coating not only improved the fluorescence stability of Yb/Tm/GZO but also enhanced the UCL intensity of Yb/Tm/GZO upconversion nanoparticles.

BIOLOGICAL TOXICITY PROPERTIES

Cytotoxicity Test of Yb/Tm/GZO@SiO_2. Yb/Tm/GZO@SiO_2 nanoparticles have potential applications in bioprobes due to their strong UCL and good biocompatibility. However, biotoxicity plays an important role in the development of nanocrystals for biological applications. Herein, the cytotoxicity of the Yb/Tm/GZO@SiO_2 core/shell UCNPs was measured. The human hepatic cell line 7702 is one of the most common human normal cell lines. The human hepatic tumor cell line HpG2 is one of the most representative human tumor cell systems. Therefore, a CCK8 assay with 7702 cells and HpG2 cells was used to investigate the cytotoxicity of Yb/Tm/GZO@SiO_2 nanoparticles (Figure 4). The 7702 and HpG2 cell viability can be quantified using eq 3.

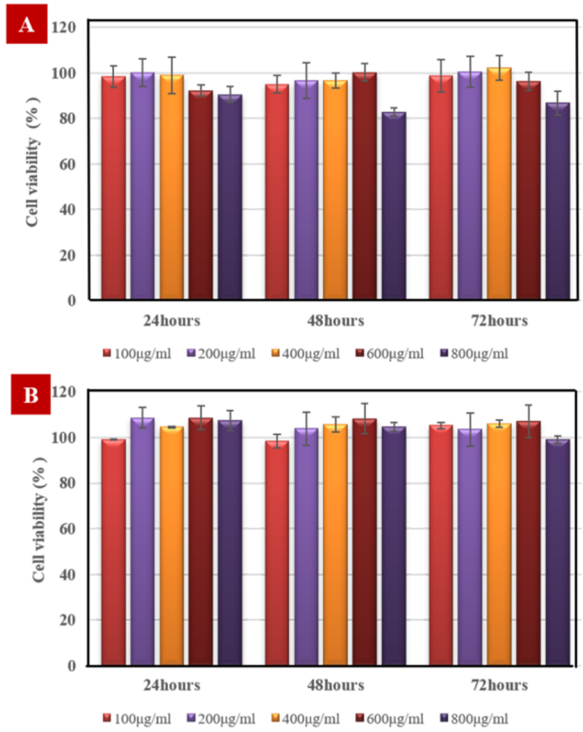

Figure 4. (A) 7702 cell viability after incubating with different charged Yb/Tm/GZO@SiO_2 concentrations ranging from 100 to 800 μg/mL for 24, 48, and 72 h. (B) HpG2 cell viability after incubating with different charged Yb/Tm/GZO@SiO_2 concentrations ranging from 100 to 800 μg/mL for 24, 48, and 72 h.

$$\text{cell viability (\%)} = \frac{A_s - A_b}{A_c - A_b} \times 100\% \quad (3)$$

where A_s is the absorbance of test cells with Yb/Tm/GZO@SiO_2 nanocomposites, and A_b and A_c stand for the absorbance of control cells without (Yb/Tm/GZO@SiO_2) nanocomposites and the absorbance of blank samples containing the culture medium (without cells and (Yb/Tm/GZO@SiO_2)), respectively. As shown in Figure 4A, the viability of 7702 cells showed no significant difference at different concentrations of 100−800 μg/mL Yb/Tm/GZO@SiO_2 for 24, 48, and 72 h. After incubating as high as 800 μg/mL of Yb/Tm/GZO@SiO_2 for 24 h, the cell viabilities were greater than 90.48%. The cell viabilities of 7702 cells kept 86.69%, despite the existence of a high concentration of 800 μg/mL and a long time of 72 h. As shown in Figure 4B, the viability of HpG2 was 99.17% after treatment of 100 μg/mL of Yb/Tm/GZO@SiO_2 for 24 h. The cellular viabilities were estimated to be greater than 99.15% with a high dosage 800 μg/mL and 72 h. These results proved that the Yb/Tm/GZO@SiO_2 core/shell had low cytotoxicity, suggesting Yb/Tm/GZO@SiO_2 as a good bioimaging probe.

In Vivo Toxicity Test of Yb/Tm/GZO@SiO_2. To further study the in vivo toxicity of Yb/Tm/GZO@SiO_2 nanoparticles, blood biochemical indexes were examined in

https://dx.doi.org/10.1021/acsomega.9b04381
ACS Omega 2020, 5, 5346−5355

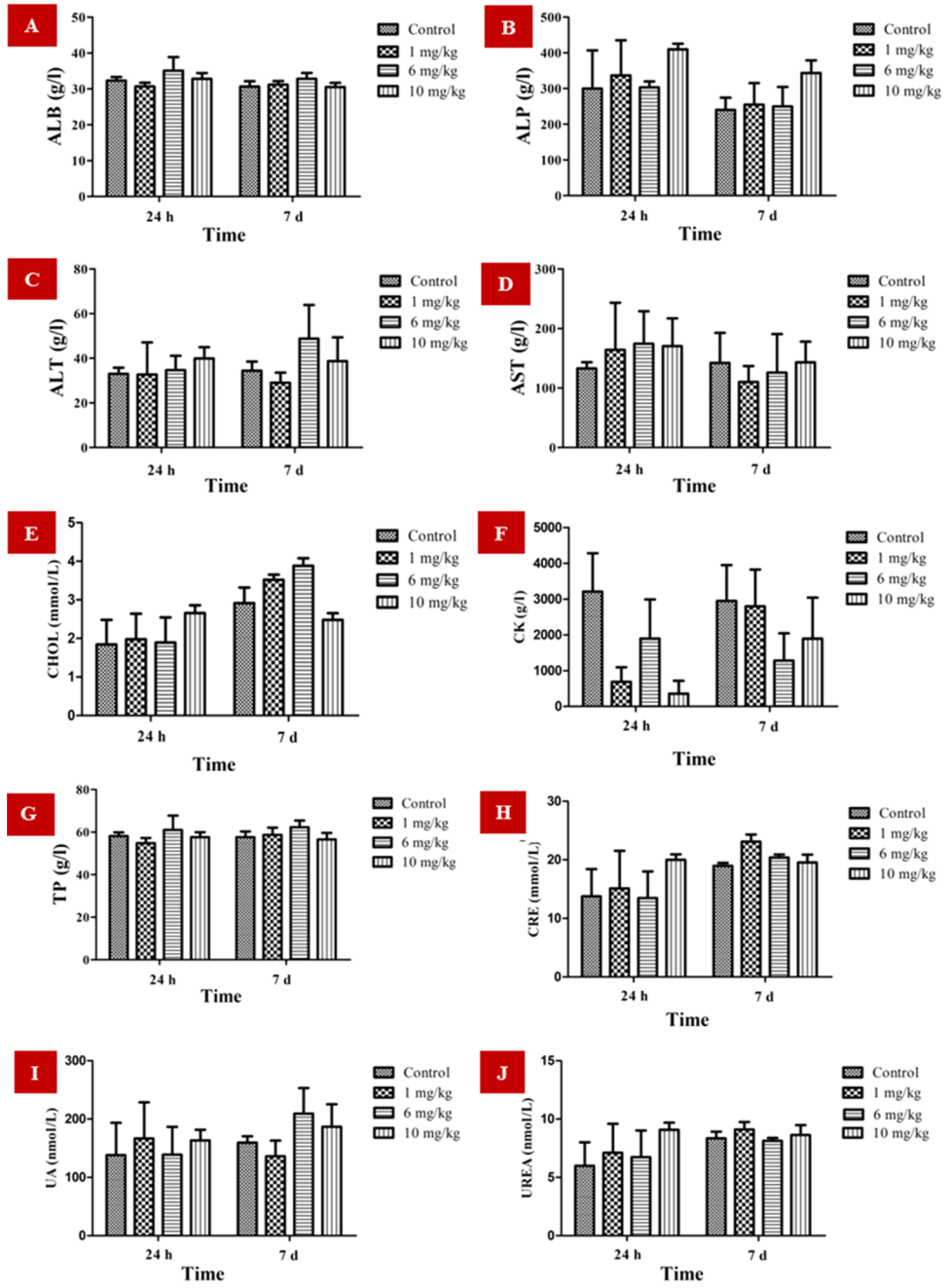

Figure 5. Serum levels after tail vein injection with Yb/Tm/GZO@SiO_2 with different concentrations (1−10 mg/kg) at 24 h and 7 days. (A) albumin (ALB); (B) alkaline phosphatase (ALP); (C) alanine transaminase (ALT); (D) aspartate aminotransferase (AST); (E) cholesterol (CHOL); (F) creatine kinase (CK); (G) total protein (TP); (H) creatinine (CRE); (I) uric acid (UA); (J) urea (UREA). Standard error of mean (SEM). Note: all data are presented as mean ± SEM (n = 8).

Kunming mouse with injecting different doses of Yb/Tm/GZO@SiO_2 through the tail vein (Figure 5). The levels of albumin (ALB), alkaline phosphatase (ALP), alanine aminotransferase (ALT), aspartate aminotransferase (AST), and cholesterol (CHOL) were related to the degree of liver cell damage, which was used as indicators to assess the function of the liver. Compared to that of control, the serum levels of ALB, ALP, ALT, AST, and CHOL had no significant change with increasing Yb/Tm/GZO@SiO_2 from 1 to 10 mg/kg (Figure 5A−E) for 24 h and 7 days post-injection. The result of the serum aminotransferases (ALB, ALP, ALT, and AST) revealed that injection with Yb/Tm/GZO@SiO_2 nanoparticles had no obvious liver injury. As shown in Figure 5H−J, the levels of serum creatinine (CRE), uric acid (UA), and urea (UREA) were further studied to identify nephrotoxicity after treating with 1−10 mg/kg Yb/Tm/GZO@SiO_2 for 24 h and 7 days. The results showed that Yb/Tm/GZO@SiO_2 had no effect on the levels of CRE, UA, or UREA in serum, indicating that injection with Yb/Tm/GZO@SiO_2 did not cause obvious damage to the nephro. In addition, the degree of creatine kinase (CK) was used to evaluate damage to the heart. As shown in Figure 5F, even after 7 days of injection with Yb/Tm/GZO@SiO_2 at a concentration as high as 10 mg/kg, the levels of serum CK had no obvious change compared to the control group, suggesting that Yb/Tm/GZO@SiO_2 injection had no obvious damage to the heart. Meanwhile, the levels of

https://dx.doi.org/10.1021/acsomega.9b04381
ACS Omega 2020, 5, 5346−5355

Table 1. Coefficients of Organs to Body Weight of Kuming Mice at 24 h and 7 days after Tail Vein Injection of Three Doses of Yb/Tm/GZO@SiO_2[a]

dose Yb/Tm/GZO@SiO_2 (mg/kg)	24 h after injection				7 days after injection			
	heart (mg/g)	liver (mg/g)	kidney (mg/g)	spleen (mg/g)	heart (mg/g)	liver (mg/g)	kidney (mg/g)	spleen (mg/g)
control	5.01 ± 0.87	57.95 ± 4.85	6.70 ± 1.31	5.61 ± 1.16	5.26 ± 0.58	76.88 ± 13.06	8.19 ± 0.36	5.46 ± 0.63
1	4.27 ± 0.21	58.14 ± 3.88	6.61 ± 0.66	4.79 ± 1.01	5.31 ± 0.58	64.26 ± 10.59	6.68 ± 0.85	4.14 ± 0.43
6	5.35 ± 0.09	55.91 ± 4.77	6.19 ± 0.73	4.28 ± 1.16	5.74 ± 1.32	69.28 ± 4.54	7.62 ± 1.31	3.76 ± 1.49
10	7.09 ± 0.21	55.33 ± 3.61	6.53 ± 0.86	3.29 ± 2.09	5.01 ± 1.22	61.68 ± 3.17	8.31 ± 0.55	3.87 ± 0.85

[a]All data are presented as mean ± standard error of the mean (SEM). (n = 8); [a]p > 0.05 versus control according to ANOVA.

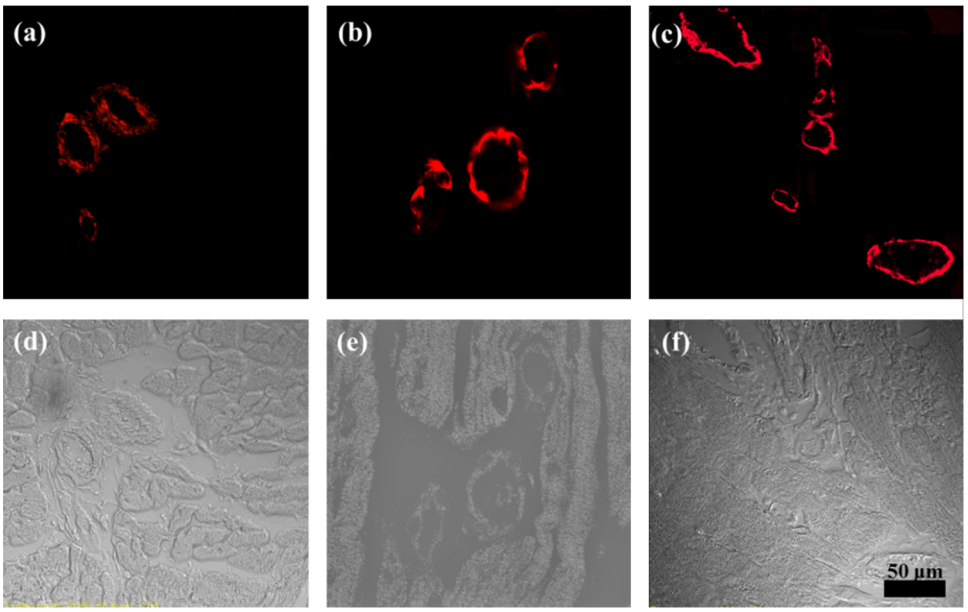

Figure 6. Confocal imaging (top) and bright-field (bottom) images of myocardial tissue following 24 h incubation with different Yb/Tm/GZO@SiO_2 contents. (a, d) 1 mg/kg, (b, e) 6 mg/kg, and (c, f) 10 mg/kg. The excitation at 980 nm was provided from a pulsed laser, and the red emission was captured by channel set at 640−660 nm (120 × 10 oil lens, scale bar = 50 μm).

serum total protein (TP) were similar for the mouse injected with Yb/Tm/GZO@SiO_2 and for the control mouse (Figure 5G). It was proved that Yb/Tm/GZO@SiO_2 UCNPs had low toxicity in vivo, indicating their potential for biological applications.

To further determine the possible tissue toxicity, histological assessments of representative organs such as the heart, liver, kidney, and spleen were performed, as shown in Table 1. Daily behavior of the Kuming mice, including drinking, eating, and activity, in the Yb/Tm/GZO@SiO_2-injected groups was identical to that in the control group. As shown in Table 1, there was no significant effect on the coefficients of the liver, kidney, and spleen 24 h after injection of Yb/Tm/GZO@SiO_2 nanoparticles. Compared to the control groups (5.01 ± 0.87 mg/g), the coefficient of the heart was slightly increased (7.09 ± 0.21 mg/g) 24 h after the tail vein injection of 10 mg/kg Yb/Tm/GZO@SiO_2 nanoparticles but without statistical significance ([a]p > 0.05). The coefficients of the heart, liver, kidney, and spleen had no apparent change after 7 days of injection with Yb/Tm/GZO@SiO_2 at all dosages (1−10 mg/kg). These results demonstrate that Yb/Tm/GZO@SiO_2 nanoparticles have low tissue toxicity and great potential applications for bioimaging.

From the analysis of tissue toxicity, we found that the coefficient of the heart was slightly increased. To assess the in vivo tissue imaging of Yb/Tm/GZO@SiO_2 nanoparticles, confocal imaging of heart tissue was studied, as shown in Figure 6. The heart was dissected out and fresh-frozen in the optimal cutting temperature (OCT) embedding medium (Sakura Finetechnical Co., Tokyo, Japan) Sections of 10 μm were cut from frozen blocks at −20 °C. Confocal imaging was done using an OLYMPUS FV500 laser scanning confocal microscope, and their upconversion luminescence was captured by channels set at 640−660 nm for receiving red upconversion emission. Figure 6 shows the multiphoton confocal imaging of heart tissue treated with 1−10 mg/kg Yb/Tm/GZO@SiO_2 following excitation at 980 nm using a femtosecond pulsed laser. The 650 nm emission (red color) of Yb/Tm/GZO@SiO_2 under 980 nm excitation was detected. Furthermore, with increasing injection concentrations of Yb/Tm/GZO@SiO_2, remarkably enhanced bright red luminescence was achieved, demonstrating that Yb/Tm/GZO@SiO_2 can effectively improve heart tissue imaging. These results suggested that Yb/Tm/GZO@SiO_2 nanoparticles showed excellent ability in bioimaging applications.

CONCLUSIONS

In summary, we demonstrated the effect of different TEOS concentrations on upconversion luminescence properties of Yb/Tm/GZO@SiO_2. With 0.6 mL of TEOS, the UCL intensity of Yb/Tm/GZO@SiO_2 enhanced about 13 times compared to that of Yb/Tm/GZO. SiO_2 coating enhanced the

https://dx.doi.org/10.1021/acsomega.9b04381
ACS Omega 2020, 5, 5346−5355

UCL stability and biocompatibility of Yb/Tm/GZO, which achieved red light imaging of heart tissue in vivo. In addition, the red fluorescence imaging of heart tissue gradually brightened with increasing injection concentrations of Yb/Tm/GZO@SiO_2 from 1 to 10 mg/kg. In vitro toxicity results indicated that Yb/Tm/GZO@SiO_2 had no significant influence on the cellular viabilities of 7702 cells and HpG2 cells after 72 h incubation with Yb/Tm/GZO@SiO_2 (100−800 μg/mL). In vivo toxicity results indicated that injection with Yb/Tm/GZO@SiO_2 nanoparticles had no obvious liver and kidney injury. The histological assessments of representative organs suggested that injection of Yb/Tm/GZO@SiO_2 nanoparticles had no significant effect on the coefficients of the heart, liver, kidney, and spleen. These studies provided that Yb/Tm/GZO@SiO_2 nanoparticles have low biotoxicity and high-resolution red tissue imaging.

EXPERIMENTAL SECTION

Materials. All chemical materials, ytterbium nitrate pentahydrate ($Yb(NO_3)_3{\cdot}5H_2O$, 99.99%), thulium nitrate pentahydrate ($Tm(NO_3)_3{\cdot}5H_2O$, 99.99%), zinc nitrate hexahydrate ($Zn(NO_3)_2{\cdot}6H_2O$, 99.9%), gallium nitrate ($Ga(NO_3)_3{\cdot}xH_2O$, 99.99%), isopropyl alcohol, tetraethyl orthosilicate (TEOS), citric acid sodium, ammonia ($NH_3{\cdot}H_2O$, 25%), and sodium hydroxide (NaOH) were used directly as received without further purification.

Synthesis of Yb/Tm/GZO. A hydrothermal method was followed: $Zn(NO_3)_2{\cdot}6H_2O$ (0.5 mmol), deionized (DI, 10 mL) water, and $Ga(NO_3)_3{\cdot}xH_2O$ (10 mol %) were dissolved by magnetic stirring for 30 min, and citric acid sodium was added to form a clarified liquid by magnetic stirring for 20 min. NaOH (2 mol/L, 10 mL) was added into the above clarified liquid to form a suspension solution by magnetic stirring for 30 min. $Tm(NO_3)_3{\cdot}5H_2O$ (with 0.5 mol %, 5 mL) and $Yb(NO_3)_3{\cdot}5H_2O$ (7 mol %, 5 mL) were added into the suspension solution by magnetic stirring for 60 min. Subsequently, the solution was transferred into a 50 mL hydrothermal reactor. The solution was heated to 150 °C for 24 h. The resultant solution was cooled down and cleaned by centrifuge at 3500 rpm for 15 min with copious amounts of ethanol and DI water. Yb/Tm/GZO was obtained by oven drying at 60 °C for 24 h.

Synthesis of Yb/Tm/GZO@SiO_2. Isopropyl alcohol (40 mL) was added to Yb/Tm/GZO (0.1713 g) by ultrasonication for 30 min to form a suspension solution. DI water (10 mL) was added into the mixture by magnetic stirring for 10 min. $NH_3{\cdot}H_2O$ (5 mL, 25%) was dropped into the suspension solution at 32 °C by magnetic stirring for 20 min. TEOS was dropped slowly into the above solution at 32 °C by magnetic stirring for 90 min. The amounts of TEOS were 0.36, 0.45, 0.60, and 0.90 mL, respectively. The resultant solution was cooled down to room temperature. The solution was washed six times with copious amounts of ethanol and DI water by centrifuge at 3500 rpm. The products were collected after oven drying at 80 °C for 24 h.

Characterization. Powder X-ray diffraction (XRD) pattern measurements were performed with Cu Kα radiation (λ = 1.54 Å). Size and morphologies of UCNPs were determined at 15 kV using a focus voltage SU8000 scanning electron microscope (SEM) and at 200 kV using a focus voltage JEOL 2010F transmission electron microscope (TEM). The upconversion emission spectra of the nanoparticles were measured at 980 nm excitation. A signal generator was used to convert a continuous 980 nm excitation source to a pulse excitation source. The upconversion spectra of samples used 980 nm as the excitation source. The excitation density was 0.3 W/cm^2. The excitation source was focused on the sample through a convex lens and became an upconversion luminous source. The source point was the sample output upconversion fluorescence. The upconversion fluorescence was absorbed by a photomultiplier tube through a set of lenses. The photomultiplier tube type was CR131, which could reach the test compensation of 1 nm, expand the light signal, and then pass through. When the receiver receives the signal and transmits the data to the connected computer, the upconversion fluorescence spectrum of a certain band would appear on the computer.

The decay lifetime of the sample was obtained on a computer with a 980 nm laser, MD03024 Mixed Domain Oscilloscope. The excitation density was 0.3 W/cm^2. The integrating sphere was used to obtain the QY of UCNPs.

Cytotoxicity Assay. The normal human hepatic cell line (7702) and the human HpG2 were cultured in the RPMI 1640 medium containing 10% fetal bovine serum. The normal human hepatic cell line (7702) and the human HpG2 were cultured in RPMI 1640 (HyClone, Thermo Fisher, Beijing, China) medium containing 10% fetal bovine serum and 1% penicillin−streptomycin. Cells were maintained in a humidified incubator (Thermo Forma) containing 5% CO_2 at 37°C, and all of the experiments were performed in a clean atmosphere. A CCK8 kit (Beyotime, Shanghai, China) was used for cell viability assay. A total of 5 × 10^3 cells/well were seeded into 96-well plates and incubated at 37 °C for 24 h. Yb/Tm/GZO@SiO_2 in the RPMI 1640/DMEM medium was added at final concentrations of 100, 200, 400, 600, and 800 μg/mL. At the end of the fixed incubation period (24, 48, and 72 h), 10 μL of the CCK8 reagent was added to each well and incubated for 4 h at 37 °C. The absorbance was recorded using a pan-wavelength microplate reader at 450 nm (Synergy Mx; BioTek, Winooski, VT). Each experiment was performed in triplicate. The cell viability can be quantified using the following equation.

$$\text{cell viability (\%)} = \frac{A_s - A_b}{A_c - A_b} \times 100\%$$

where A_s is the absorbance of the test sample (test wells containing cells, culture medium, and samples), A_b is the absorbance of the control sample (control wells containing cells and culture medium without samples), and A_c is the absorbance of blank samples (blank wells containing the culture medium without cell and samples).

In Vivo Toxicity and Imaging Studies. All animal experiments and procedures were approved by the Animal Ethical and Experimental Committee of the Tianjin Medical University Metabolic Diseases Hospital. Five-week-old male Kunming mice (23−26 g) were purchased from the animal center of Military Medical Sciences Academy of the PLA (Permission no SCXK-(A) 2012-0004). All experimental mice were maintained in a 12 h light/12 h dark cycle at 22 °C and 55 ± 5% relative humidity in a standard laboratory room at Tianjin Medical University (Tianjin, China). The mice were provided rodent chow and water ad libitum.

After a week of acclimation, the mice were randomly allocated into four groups (eight animals in each group): three sample groups (treated with final doses 1, 6, and 10 mg/kg of the Yb/Tm/GZO@SiO_2 body weight) and a vehicle group

https://dx.doi.org/10.1021/acsomega.9b04381
ACS Omega 2020, 5, 5346−5355

(treated with an equivalent volume of phosphate-buffered saline (PBS)). Yb/Tm/GZO@SiO_2 nanoparticles and PBS were injected via the tail vein. Eight mice from each group were weighed and sacrificed by CO_2 asphyxiation after 24 h and 7 days. Serum samples were collected by centrifugation (3000*g*, 10 min). ALB, ALP, ALT, AST, CHOL, CK, TP, CRE, UA, and UREA were detected according to the kit's protocol (Roche, People's Republic of China). Liver, lung, spleen, kidney, and heart samples were collected and weighed. The heart was dissected out and fresh-frozen in the OCT embedding medium (Sakura Finetechnical Co, Tokyo, Japan). Sections of 10 μm were cut from frozen blocks at −20 °C, and confocal microscopy was used to observe the imaging of cardiac myocytes. Confocal imaging was done using an OLYMPUS FV500 laser scanning confocal microscope (120 × 10 oil lens), and their upconversion luminescence was captured by channels set at 640−660 nm for receiving red upconversion emission at 980 nm using a femtosecond pulsed laser under an excitation of 0.3 W/cm^2.

■ ASSOCIATED CONTENT

Supporting Information

The Supporting Information is available free of charge at https://pubs.acs.org/doi/10.1021/acsomega.9b04381.

Log−log plots of the intensity versus input pump power for the blue UC and red UC emissions in Yb/Tm/GZO, and the blue and red UC luminescence mechanism of Yb/Tm/GZO nanocrystals under 980 nm excitations (PDF)

■ AUTHOR INFORMATION

Corresponding Author

Yandong Bai − *Tianjin Union Medical Center, 300121 Tianjin, China;* orcid.org/0000-0001-7241-9626; Email: baiyandong0821@sina.com

Authors

Yuemei Li − *School of Chemistry and Chemical Engineering, Harbin Institute of Technology, Harbin, Heilongjiang 150001, China*

Rui Wang − *School of Chemistry and Chemical Engineering, Harbin Institute of Technology, Harbin, Heilongjiang 150001, China;* orcid.org/0000-0002-1964-4776

Yongmei Li − *NHC Key Laboratory of Hormones and Development (Tianjin Medical University), Tianjin Key Laboratory of Metabolic Diseases, Tianjin Medical University Chu Hsien-I Memorial Hospital, Tianjin Institute of Endocrinology, Tianjin 300134, China;* orcid.org/0000-0003-1808-6060

Complete contact information is available at: https://pubs.acs.org/10.1021/acsomega.9b04381

Notes

The authors declare no competing financial interest.

■ ACKNOWLEDGMENTS

This work was financially supported by the Science & Technology Development Fund of Tianjin Education Commission for Higher Education (No. 2018KJ069) and Startup Funding of Scientific Research, Tianjin Medical University Metabolic Diseases Hospital and Tianjin Institute of Endocrinology (No. 2017DX07).

■ REFERENCES

(1) Nyk, M.; Kumar, R.; Ohulchanskyy, T. Y.; Bergey, E. J.; Prasad, P. N. High contrast in vitro and in vivo photoluminescence bioimaging using near infrared to near infrared up-conversion in Tm^{3+} and Yb^{3+} doped fluoride nanophosphors. *Nano Lett.* **2008**, *8*, 3834−3838.

(2) Zhou, J.; Sun, Y.; Du, X.; Xiong, L.; Hu, H.; Li, F. Dual-modality in vivo, imaging using rare-earth nanocrystals with near-infrared to near-infrared (NIR-to-NIR) upconversion luminescence and magnetic resonance properties. *Biomaterials* **2010**, *31*, 3287−3295.

(3) Haun, J. B.; Devaraj, N. K.; Marinelli, B. S.; Lee, H.; Weissleder, R. Probing Intracellular Biomarkers and Mediators of Cell Activation Using Nanosensors and Bioorthogonal Chemistry. *ACS Nano* **2011**, *5*, 3204−3213.

(4) Sharma, P.; Brown, S.; Walter, G.; Santra, S.; Moudgil, B. Nanoparticles for bioimaging. *Adv. Colloid Interface Sci.* **2006**, *123−126*, 471−485.

(5) Pan, D.; Caruthers, S. D.; Chen, J.; Winter, P. M.; SenPan, A.; Schmieder, A. H.; Wickline, S. A.; Lanza, G. M. Nanomedicine strategies for molecular targets with MRI and optical imaging. *Future Med. Chem.* **2010**, *2*, 471−490.

(6) Castro, P. d. P.; Curi, N.; Furtini, N. A. E. Chemistry and mineralogy of soils cultivated with *Eucalyptus* (*Eucalyptus* sp.). *Scientia Forestalis* **2010**, *6*, 71.

(7) Hemmilä, I.; Laitala, V. Progress in lanthanides as luminescent probes. *J. Fluoresc.* **2005**, *15*, 529−542.

(8) Bokolia, R.; Mondal, M.; Rai, V. K.; Sreenivas, K. Enhanced infrared-to-visible up-conversion emission and temperature sensitivity in (Er^{3+}, Yb^{3+}, and W^{6+}) tri-doped $Bi_4Ti_3O_{12}$ ferroelectric oxide. *J. Appl. Phys.* **2017**, *121*, No. 084101.

(9) Chen, D.; Xu, M.; Huang, P. Core@shell upconverting nanoarchitectures for luminescent sensing of temperature. *Sens. Actuators, B* **2016**, *231*, 576−583.

(10) Park, Y. I.; Nam, S. H.; Kim, J. H.; Bae, Y. M.; Yoo, B.; Kim, H. M.; Jeon, K.-S.; Park, H. S.; Choi, J. S.; Lee, K. T.; Suh, Y. D.; Hyeon, T. Comparative Study of upconverting Nanoparticles with Various Crystal Structures, Core/Shell Structures, and Surface Characteristics. *J. Phys. Chem. C* **2013**, *117*, 2239−2244.

(11) Hildebrandt, N.; Lohmannsroben, H. G. Quantum Dot nanocrystals and Supramolecular Lanthanide Complexes -Energy Transfer Systems for Sensitive In Vitro Diagnostics and High Throughput Screening in Chemical Biology. *Curr. Chem. Biol.* **2007**, *1*, 167−186.

(12) Ruan, G.; Agrawal, A.; Marcus, A. I.; Nie, S. Imaging and Tracking of Tat Peptide-Conjugated Quantum Dots in Living Cells: New Insights into Nanoparticle Uptake, Intracellular Transport, and Vesicle Shedding. *J. Am. Chem. Soc.* **2007**, *129*, 14759−14766.

(13) Haun, J. B.; Devaraj, N. K.; Marinelli, B. S.; Lee, H.; Weissleder, R. Probing Intracellular Biomarkers and Mediators of Cell Activation Using Nanosensors and Bioorthogonal Chemistry. *ACS Nano* **2011**, *5*, 3204−3213.

(14) Yu, M.; Li, F.; Chen, Z.; Hu, H.; Zhan, C.; Yang, H.; Huang, C. Laser scanning up-conversion luminescence microscopy for imaging cells labeled with rare-earth nanophosphors. *Anal. Chem.* **2009**, *81*, 930−935.

(15) Xiong, L.; Chen, Z.; Tian, Q.; Cao, T.; Xu, C.; Li, F. High contrast upconversion luminescence targeted imaging in vivo using peptide-labeled nanophosphors. *Anal. Chem.* **2009**, *81*, 8687−8694.

(16) Wang, M.; Mi, C.-C.; Wang, W.-X.; Liu, C.-H.; Wu, Y.-F.; Xu, Z.-R.; Mao, C.-B.; Xu, S.-K. Immunolabeling and NIR-Excited Fluorescent Imaging of HeLa Cells by Using $NaYF_4$:Yb,Er upconversion Nanoparticles. *ACS Nano* **2009**, *3*, 1580−1586.

(17) Wang, F.; Banerjee, D.; Liu, Y.; Chen, X.; Lu, X. Upconversion nanoparticles in biological labeling, imaging, and therapy. *Analyst* **2010**, *135*, 1839−1854.

(18) Tian, G.; Gu, Z.; Zhou, L.; et al. Mn^{2+} dopant-controlled synthesis of $NaYF_4$:Yb/Er upconversion nanoparticles for in vivo imaging and drug delivery. *Adv. Mater.* **2012**, *24*, 1226−1231.

(19) Wen, S.; Zhou, J.; Zheng, K.; Bednarkiewicz, A.; Liu, X.; Jin, D. Advances in highly doped upconversion nanoparticles. *Nat. Commun.* **2018**, *9*, No. 2415.
(20) Dacosta, M. V.; Doughan, S.; Han, Y.; Krull, U. J. Lanthanide upconversion nanoparticles and applications in bioassays and bioimaging: A review. *Anal. Chim. Acta* **2014**, *832*, 1−33.
(21) Kumar, A.; Reddy, K. R.; Kumar, S.; Kumar, A.; Sharma, V.; Krishnan, V. Rational design and development of lanthanide-doped $NaYF_4$@CdS-Au-RGO as quaternary plasmonic photocatalysts for harnessing visible-near-infrared broadband spectrum. *ACS Appl. Mater. Interfaces* **2018**, *10*, 15565−15581.
(22) Wang, H.; Han, R.-l.; Yang, L.-m.; Shi, J.-h.; Liu, Z.-j.; Hu, Y.; Wang, Y.; Liu, S.-j.; Gan, Y. Design and synthesis of core-shell-shell upconversion nanoparticles for NIR-induced drug release, photodynamic therapy, and cell imaging. *ACS Appl. Mater. Interfaces* **2016**, *8*, 4416−4423.
(23) Lingeshwar Reddy, K. L.; Srinivas, V.; Shankar, K. R.; et al. Enhancement of luminescence intensity in red Emitting $NaYF_4$:Yb/Ho/Mn upconversion nanophosphors by variation of reaction parameters. *J. Phys. Chem. C* **2017**, *121*, 11783−11793.
(24) Auzel, F. Upconversion and anti-Stokes processes with f and d ions in solids. *ChemInform* **2004**, *35*, 139−174.
(25) Wilhelm, S.; Kaiser, M.; Würth, C.; et al. Water dispersible upconverting nanoparticles: effects of surface modification on their luminescence and colloidal stability. *Nanoscale* **2015**, *7*, 1403−1410.
(26) Cen, Y.; Wu, Y.-M.; Kong, X.-J.; Wu, S.; Yu, R.-Q.; Chu, X. Phospholipid-modified upconversion nanoprobe for ratiometric fluorescence detection and imaging of phospholipase D in cell lysate and in living cells. *Anal. Chem.* **2014**, *86*, 7119−7127.
(27) Mani, K. P.; Vimal, G.; Biju, P. R.; Unnikrishnan, N. V.; Ittyachen, M. A.; Joseph, C. Synthesis and optical characterization of host sensitized color tunable $Tb_{2-x}Eu_x(MoO_4)_3$ nanophosphors for optoelectronic applications. *J. Mater. Sci.: Mater. Electron.* **2016**, *27*, 966−975.
(28) Haase, M.; Schäfer, H. Upconverting nanoparticles. *Angew. Chem., Int. Ed.* **2011**, *50*, 5808−5829.
(29) Hilderbrand, S. A.; Shao, F.; Salthouse, C.; Mahmood, U.; Weissleder, R. Upconverting luminescent nanomaterials: application to in vivo bioimaging. *Chem. Commun.* **2009**, *28*, 4188−4190.
(30) Alkahtani, M. H.; Alghannam, F. S.; Sanchez, C.; Gomes, C. L.; Liang, H.; Hemmer, P. R. High efficiency upconversion nanophosphors for high-contrast bioimaging. *Nanotechnology* **2016**, *27*, No. 485501.
(31) Luo, W.; Li, R.; Liu, G.; Antonio, M. R.; Chen, X. Evidence of Trivalent Europium Incorporated in anatase TiO_2 nanocrystals with Multiple Sites. *J. Phys. Chem. C* **2008**, *112*, 10370−10377.
(32) Luo, W.; Li, R.; Chen, X. Host-Sensitized Luminescence of Nd^{3+} and Sm^{3+} Ions Incorporated in anatase titania nanocrystals. *J. Phys. Chem. C* **2009**, *113*, 8772−8777.
(33) Planelles-Aragó, J.; Julián-López, B.; Cordoncillo, E.; et al. Lanthanide doped ZnS quantum dots dispersed in silica glasses: An easy one pot sol-gel synthesis for obtaining novel photonic materials. *J. Mater. Chem.* **2008**, *18*, 5193−5199.
(34) Bahtat, A.; Bouazaoui, M.; Bahtat, M.; Garapon, C.; Jacquier, B.; Mugnier, J. Up-conversion fluorescence spectroscopy in Er^{3+}:TiO_2 planar waveguides prepared by a sol-gel process. *J. Non-Cryst. Solids* **1996**, *202*, 16−22.
(35) Wang, C.; Cheng, L.; Liu, Y.; et al. Imaging-guided pH-sensitive photodynamic therapy using charge reversible upconversion nanoparticles under near−infrared light. *Adv. Funct. Mater.* **2013**, *23*, 3077−3086.
(36) Park, Y. I.; Kim, J. H.; Kang, T. L.; et al. Nonblinking and nonbleaching upconverting nanoparticles as an optical imaging nanoprobe and T1 magnetic resonance imaging contrast agent. *Adv. Mater.* **2009**, *21*, 4467−4471.
(37) Achatz, D. E.; Meier, R. J.; Fischer, L. H.; Wolfbeis, O. S. Luminescent sensing of oxygen using a quenchable probe and upconverting nanoparticles. *Angew. Chem., Int. Ed.* **2011**, *50*, 260−263.
(38) Frindell, K. L.; Bartl, M. H.; Popitsch, A.; Stucky, G. D. Sensitized luminescence of trivalent europium by three-dimensionally arranged anatase nanocrystals in mesostructured titania thin films. *Angew. Chem., Int. Ed.* **2002**, *41*, 959−962.
(39) Ji, S.; Yin, L.; Liu, G.; Zhang, L.; Ye, C. Synthesis of Rare Earth Ions-Doped ZnO Nanostructures with Efficient Host−Guest Energy Transfer. *J. Phys. Chem. C* **2009**, *113*, 16439−16444.
(40) Wang, F.; Han, Y.; Lim, C. S.; et al. Simultaneous phase and size control of upconversion nanocrystals through lanthanide doping. *Nature* **2010**, *463*, 1061−1065.
(41) Chen, G.; Qiu, H.; Prasad, P. N.; Chen, X. Upconversion nanoparticles: Design, nanochemistry, and applications in theranostics. *Chem. Rev.* **2014**, *114*, 5161−5214.
(42) Arvizo, R. R.; Miranda, O. R.; Thompson, M. A.; et al. Effect of nanoparticle surface charge at the plasma membrane and beyond. *Nano Lett.* **2010**, *10*, 2543−2548.
(43) Verma, A.; Stellacci, F. Effect of surface properties on nanoparticle-cell interactions. *Small* **2010**, *6*, 12−21.
(44) Asati, A.; Santra, S.; Kaittanis, C.; Manuel Perez, J. Surface-Charge-Dependent Cell Localization and Cytotoxicity of Cerium Oxide Nanoparticles. *ACS Nano* **2010**, *4*, 5321−5331.
(45) Jin, J.; Gu, Y.-J.; Man, C. W.-Y.; et al. Polymer-coated $NaYF_4$:Yb^{3+}, Er^{3+} upconversion nanoparticles for charge-dependent cellular imaging. *ACS Nano* **2011**, *5*, 7838−7847.
(46) Conner, S. D.; Schmid, S. L. Regulated portals of entry into the cell. *Nature* **2003**, *422*, 37−44.
(47) Reddy, K. L.; Sharma, P. K.; Singh, A.; Kumar, A.; Shankar, K. R.; Singh, Y.; Garg, N.; Krishnan, V. Amine-functionalized, porous silica-coated $NaYF_4$:Yb/Er upconversion nanophosphors for efficient delivery of doxorubicin and curcumin. *Mater. Sci. Eng., C* **2019**, *96*, 86−95.
(48) Reddy, K. L.; Kumar, S.; Kumar, A.; Krishnan, V. Wide spectrum photocatalytic activity in lanthanide-doped upconversion nanophosphors coated with porous TiO_2 and Ag-Cu bimetallic nanoparticles. *J. Hazard. Mater.* **2019**, *367*, 694−705.
(49) Lü, Q.; Li, A.; Guo, F.; Sun, L.; Zhao, L. The two-photon excitation of SiO_2-coated Y_2O_3:Eu^{3+} nanoparticles by a near-infrared femtosecond laser. *Nanotechnology* **2008**, *19*, No. 205704.
(50) Wu, S.; Duan, N.; Shi, Z.; Fang, C.; Wang, Z. Simultaneous aptasensor for multiplex pathogenic bacteria detection based on multicolor upconversion nanoparticles labels. *Anal. Chem.* **2014**, *86*, 3100.
(51) Zhao, L.; Peng, J.; Huang, Q.; et al. Near-Infrared Photoregulated Drug Release in Living Tumor Tissue via Yolk-Shell upconversion Nanocages. *Adv. Funct. Mater.* **2014**, *24*, 363−371.
(52) El-Toni, A. M.; Yin, S.; Sato, T. Control of silica shell thickness and microporosity of titania−silica core−shell type nanoparticles to depress the photocatalytic activity of titania. *J. Colloid Interface Sci.* **2006**, *300*, 123−130.
(53) Liu, Z.; Yi, G.; Zhang, H.; Ding, J.; Zhang, Y.; Xue, J. Monodisperse silica nanoparticles encapsulating upconversion fluorescent and superparamagnetic nanocrystals. *Chem. Commun.* **2008**, *14*, 694−696.

https://dx.doi.org/10.1021/acsomega.9b04381
ACS Omega 2020, 5, 5346−5355